

UVM ScholarWorks

Optical Properties of Mesoporous Tungsten(VI) Oxide Functionalized with π -Conjugated Organic Molecules for Heterogeneous Photocatalysis

Item Type	undergrad_thesis;article;undergraduate thesis
Authors	Burke, Jack Henry
Download date	2026-06-11 10:39:08
Link to Item	https://hdl.handle.net/20.500.14849/525

Optical Properties of Mesoporous Tungsten(VI) Oxide Functionalized with π -Conjugated Organic Molecules for Heterogeneous Photocatalysis

Jack Burke

Advisor: Dr. Christopher C. Landry

Abstract

Heterogeneous photocatalysts are of interest for their use in applications such as environmental remediation. WO_3 is a known photocatalyst, and mesoporous WO_3 offers a higher surface area than the bulk material, and thus a greater concentration of active sites. By covalently attaching π -conjugated organic molecules to the surface of metal oxides, sensitization of the semiconductor is possible through charge transfer between the molecule and the solid. In this work, mesoporous WO_3 particles, synthesized *via* a hard-templating method from mesoporous SiO_2 , are modified by attachment of either folic acid or 3,3''-dihexyl-2,2':5',2'':5'',2'''-quaterthiophene (DH4T) to the surface of the particles. Covalent attachment of these molecules to the metal oxide is achieved by use of a silane anchoring group, aminopropyltriethoxysilane (APTES), which attaches to the surface by a condensation reaction with the surface hydroxides. The amine group of APTES then allows for peptide coupling with FA or the carboxylated thiophene tetramer, DH4T-COOH, yielding WO_3 -APTES-FA or WO_3 -APTES-DH4T. The optical properties of the synthesized materials were studied by photoluminescence (PL) spectroscopy under 405 nm laser excitation. WO_3 -APTES-FA showed no change in spectrum from WO_3 , possibly due to small surface concentration of the molecule, or the fact that 405 nm is not resonant with any electronic transitions of FA. WO_3 -APTES-DH4T showed an intense PL emission when excited at 405 nm. Fitting of the spectrum revealed contribution from the molecular emission, as well as transitions involving oxygen vacancy (OV) states in WO_3 . Photophysical mechanisms of the sensitization of WO_3 by DH4T are proposed, and possible implications for photocatalysis are discussed.

Introduction

Heterogeneous photocatalysts can easily be separated out a reaction mixture, and have the potential to use ambient sunlight for chemical conversions, which make them an attractive system for degradation of pollutants in waterways. Semiconductor metal oxides are among the most popular heterogeneous photocatalysts. The active sites of these catalysts exist on the surface of the material. Porous microparticles are therefore attractive morphological structures for metal oxide photocatalysts, as they possess a high surface area.

Upon bandgap irradiation of a semiconductor, electron-hole pairs are created, which after separation, can diffuse to the surface and react with adsorbed species. Specifically, holes can oxidize surface-adsorbed species, and electrons can reduce surface-adsorbed species. In this manner, the photocatalyst initiates redox reactions through photogenerated, reactive charge carriers. Therefore, increasing the quantum yield of charge carriers could increase the efficiency of the catalyst.

Interfacial charge transfer is an important process that is vital to many next-generation energy storage technologies. It is ubiquitous in solar energy harvesting, in both generation of electricity, and conversion of solar energy to fuels for storage. Charge transfer between surface-tethered molecules and semiconductors has been exploited in dye-sensitized solar cells (DSSCs). In these systems, an organic or organometallic dye is anchored to the surface of a semiconductor electrode. The dyes offer large extinction coefficients, and possibly absorption at longer wavelengths than the semiconductor. Charge transfer between the dye and the electrode allow for an increase in charge carrier concentration, and thus sensitization of the semiconductor. The original oxidation state of the dye is typically restored by an electrolyte redox couple.¹

Dye sensitization has also been applied to supported molecular photoelectrocatalysts for water splitting. Water splitting is the process of converting water to the useful fuels O_2 and H_2 . These systems are coined dye-sensitized water splitting catalysts (DSWSCs). A cartoon depiction of a typical design of these systems is shown in Figure 1. The cell features a photoanode and photocathode, with supported molecular water oxidation (WO), and hydrogen generating (HG) catalysts, respectively. Both electrodes also possess a tethered molecular dye, that is able to absorb light and transfer holes (electrons) to the water oxidation (hydrogen generating) catalysts, and thus provide the oxidizing (reducing) power necessary for the water splitting reaction.²

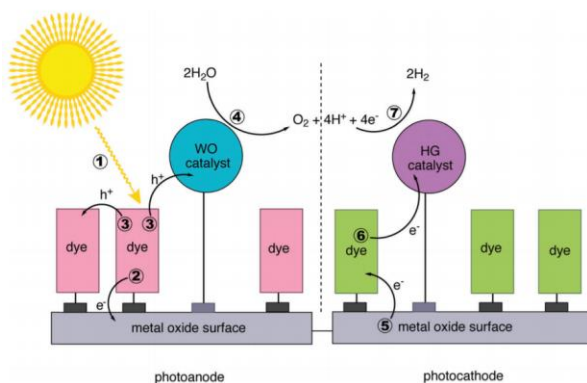


Figure 1: Simplified cartoon diagram of a dye-sensitized water splitting catalyst. Figure taken from ².

DSSCs illustrate the ability of surface-bound molecular dyes to sensitize semiconductors. DSWSCs utilize this ability to increase the redox capabilities of supported molecular catalysts. However, the effect of organic sensitizer molecules on the photocatalytic activity of semiconductor surfaces has remained unexplored. It is conceivable that charge transfer between a surface-bound dye and a semiconductor microparticle could increase the carrier concentration, and thus modify the photocatalytic activity of the semiconductor. It is the purpose of this thesis to modify semiconductor photocatalysts with organic dye molecules and investigate their

optoelectronic properties *via* photoluminescence (PL) spectroscopy. The PL spectra will provide information on the viability of dye-sensitization in semiconductor photocatalysts.

Titania (TiO_2) is a very commonly studied metal oxide heterogeneous photocatalyst. However, titania possesses a bandgap of 3.2 eV, which lies in the ultraviolet.³ The solar spectrum shows the highest intensity in the visible region, meaning that titania has limited application in photocatalysis utilizing ambient sunlight as the photon source. On the other hand, WO_3 possesses a bandgap of 2.8 eV, which lies in the visible region.³ Therefore, WO_3 will be used as the semiconductor solid in this study.

Several anchoring groups are used to tether molecules to metal oxide surfaces.¹⁻² Phosphate and carboxylate anchoring groups are commonly employed in dye-sensitized solar cells. These bind to the surface by coordination to Lewis acidic sites, as well as by electrostatic attraction if the metal oxide possesses a positive surface potential. Alternatively, trialkoxysilanes can be used as anchoring groups. Through a condensation reaction, surface hydroxides of the semiconductor can substitute for the alkoxides. This results in covalent attachment to the surface, rather than the coordinative attachment of phosphates and carboxylates. It is desired for the purposes of this study to form stable, non-labile bonds between the surface of the semiconductor and the dye. For this reason, aminopropyltriethoxysilane (APTES) will be used as a surface anchor.

Oligothiophenes have been used to sensitize TiO_2 solar cells.⁴ The tetra-, octa-, and dodecamers were carboxylated to allow for coordination to the surface. The dicarboxylic acid of the tetramer was also prepared to test the effect of having two anchoring groups on the molecule. The carboxylated oligothiophenes were adsorbed onto a TiO_2 electrode, which was then used in a solar cell. It was found that the oligothiophenes extended the incident photon-to-current

conversion efficiency (ICPE) spectrum into the visible region. The ICPE spectra of the octamer and dodecamer showed signal across a greater region of the spectrum as a result of the longer wavelength absorption due to increased conjugation. The dodecamer, however, showed lower ICPE intensity than the octamer. The tetramer, quaterthiophene, showed greater ICPE for the dicarboxylate than the carboxylate, likely due to enhanced adsorption (greater surface concentration) of the sensitizer due to possession of two anchoring groups.

Silane linkers have also been used to link sensitizers to TiO₂. Turkowski *et al.*⁵ reported appearance of an intense photoluminescence (PL) of TiO₂ nanoparticles when functionalized with folic acid (FA) molecules covalently attached *via* an aminopropyltrimethoxysilane (APTMS) anchor. It was hypothesized for this system that the intense PL observed involved charge transfer transitions between the molecular orbitals of FA and the oxygen vacancy (OV) states of TiO₂.

In the current study, it is examined mesoporous WO₃ particles functionalized by dihexylquaterthiophene (DH4T) and folic acid (FA). WO₃ is used instead of TiO₂ due to its smaller bandgap. DH4T and FA are chosen for comparison with the above described studies. The materials synthesized herein use the silane anchor APTES to covalently attach the molecule to the surface, which will allow for stable, non-labile surface modification. Photoluminescence experiments are performed on the materials to explore their photophysical properties, and help determine the applicability of the material to photocatalysis.

Experimental

Materials Characterization

N₂ physisorption experiments were carried out on a Micromeritics Tristar 2400 Surface Area and Porosity Analyzer. Surface areas and pore size distributions were calculated using the BET and BJH methods, respectively. Powder X-ray diffraction (XRD) was performed on a Rigaku MiniFlex II diffractometer using Cu K α radiation generated with a tube output voltage and current of 30 kV and 15 mA, respectively. The diffractometer was equipped with a water-cooled Scintillator detector that was used at a continuous rate of 0.5° (2 θ) per minute. Crystallite size was calculated by the Scherrer equation, where τ is the crystallite size, K is the dimensionless shape factor (taken to be 0.9), λ is the wavelength of the X-ray, β is the full width at half maximum (FWHM) of the peak, and θ is the diffraction angle (in radians):

$$\tau = \frac{K\lambda}{\beta\cos(\theta)} \quad 1)$$

Scanning electron micrographs were recorded with a JEOL JSM-6060 SEM instrument. Dry samples were dispersed on carbon tape and sputter coated with 40:60 Au/Pd prior to imaging. Thermogravimetric analysis (TGA) was performed on a PerkinElmer Pyris 1 TGA Thermogravimetric Analyzer.

Spectroscopic Experiments

UV/vis absorption spectra were recorded on a PerkinElmer Lambda 35 UV/vis spectrometer with PerkinElmer UV Winlab software. Diffuse Reflectance Spectroscopy was performed with a Labsphere RSA-PE-20 Reflectance Spectroscopy Accessory to the

PerkinElmer spectrometer. Reflectance (R) was converted to the quantity F(R), which is proportional to the extinction coefficient:⁶

$$F(R) = \frac{(1-R)^2}{2R} \quad 2)$$

Fluorescence emission spectra were recorded on a Photon Technology International QuantaMaster-4 Fluorimeter with FelixGX software.

Photoluminescence (PL) spectra were recorded using a Princeton Instruments CCD camera, coupled to a 0.5m focal length Acton spectrometer. The excitation source was a 405 nm continuous wave Coherent Cube laser, attenuated to 90 μ W at the sample. Collection of scattered source radiation background was minimized from the emission spectra by linear polarizing the excitation beam, and selectively analyzing the orthogonal component of the photoluminescence by placing a second linear polarizer in front of the entrance slit. PL samples were prepared by drop casting the particles from concentrated suspensions in ethanol onto glass microscope slides. Curve fitting of PL spectra was performed on PeakFIT. Spectra were smoothed *via* Loess regression prior to fitting.

Synthesis of Mesoporous SiO₂ Template

In a 500 mL Erlenmeyer flask, cetyltrimethylammonium bromide (CTAB, 9.0 g, 24.7mmol) was stirred at room temperature in deionized H₂O (198.0 g, 11 mol), EtOH (95 % v/v, 55.5 g, 1.14 mol), and concentrated HCl (37 % wt/wt, 22.0 g, 223.0 mol) until dissolution. Tetraethyl orthosilicate (TEOS, 20.0 g, 96.0 mmol) was added and the solution was stirred for 10 min, at which time NaF solution (0.5 M, 23.8 g, 11.9 mmol) was added. The solution was stirred until it turned opaque (approximately 1 min), then immediately transferred to a polypropylene bottle, which was then placed in a 373 K oven for 2 hr. Upon removal from the oven, the

solution was then stirred in an ice bath for 15 min. The solid was collected by filtration and washed with 30 mL of H₂O and 30 mL of EtOH. The solid was allowed to air dry overnight, then calcined with the following program: heat from 298 K to 723 K at 2 K min⁻¹, hold at 723 K for 140 min, heat from 723 K to 823 K at 10 K min⁻¹, hold at 823 K for 480 min. The resulting material is designated as SiO₂.

Impregnation of SiO₂ Template with WO₃

WO₃-SiO₂ composite materials were prepared by the method of incipient wetness. The tungsten oxide precursor solution, aqueous ammonium metatungstate (AMT, 1.5 g/mL) was added dropwise to SiO₂ powder (1 g) in a calcine dish, with thorough, intermittent stirring. The volume of AMT solution used was equal to the pore volume of the SiO₂ sample, as determined by N₂ physisorption. After addition of the total volume of AMT solution and thorough stirring, the material, now slightly clumpy, was allowed to air dry for 3 hr. The powder was then calcined by ramping to 550 °C and cooling to RT. The resulting yellow powder is designated as WO₃-SiO₂.

Etching of SiO₂ Template to Yield Mesoporous WO₃

Silica template was removed from the WO₃-SiO₂ composites *via* HF etching (warning: hydrofluoric acid is corrosive and extremely toxic). HF solution (2.89 M, 10 mL) was prepared by adding to a 15 mL centrifuge tube H₂O (8mL), then concentrated HF (49.0 % wt/wt, 28.9 M, 1 mL) followed by additional H₂O (1mL). To this solution, WO₃-SiO₂ (0.5 – 1.0 g) was added and shaken to disperse. The suspension was then shaken on a rotating platform for 4 hr. The suspension was centrifuged and the solution decanted, and the particles were then washed 3

times with H₂O (12 mL) and once with EtOH (12 mL). The particles were then dried overnight at 80 °C.

Surface Modification of WO₃ with APTES

WO₃ (1.5 g) was added to toluene (50 mL) in a 100 mL round bottom flask. The flask was sonicated to disperse the particles. An excess of APTES (1 mL, 4.27 mmol) was added, and the mixture was refluxed under N₂ for 12 hr. The particles were collected by filtration and washed with 100 mL of toluene and 200 mL of EtOH, then dried at 80 °C. A typical yield of 1.1 g was obtained.

Coupling of Organic Light-Absorbing species to APTES surface anchor

Organic sensitizer molecules were attached to the APTES surface anchor via EDC/NHS coupling. The carboxylic acid-containing sensitizer molecule (folic acid or DH4T-COOH, 1 eq.) was added to 100 mL of DMSO in a 250 mL round bottom flask. Then, to the flask, N-(3-dimethylaminopropyl)-N'-ethylcarbodiimide hydrochloride (EDC•HCl, 5 eq.) and N-hydroxysuccinimide (NHS, 5 eq.) were added. The resultant mixture was stirred for 1 hr. Then, WO₃-APTES (0.75 eq. APTES, typically 0.5 g) was added to the solution. The mixture was then sonicated for 1 min., then stirred for 12 hr. The resultant suspension was then allowed to settle then decanted to 12 mL and transferred to a 15 mL centrifuge tube. The suspension was centrifuged, decanted, and washed 3 times with DMSO (12 mL) and once with EtOH (12 mL).

Synthesis of 3,3'''-dihexyl-2,2':5',2'':5'',2'''-quaterthiophene-5-carboxylic acid

(DH4T-COOH)

To a dry 100 mL Schlenk flask under nitrogen, 3,3'''-dihexyl-2,2':5',2'':5'',2'''-quaterthiophene (0.5 g, 1.0 mmol) was added, followed by THF (39 mL). Next, the flask was

cooled to $-78\text{ }^{\circ}\text{C}$, and n-butyllithium (0.985 N, 1.101 mL, 1.0 mmol) was slowly added, causing the solution to change from orange to dark orange/ brown. The solution was stirred at room temperature for 1 hr, during which time an orange paste formed. The flask was then cooled to $-78\text{ }^{\circ}\text{C}$, and a large piece of dry ice ($\sim 8\text{ g}$) was added. The solution was allowed to stir at room temperature for another hr, before cooling to $-78\text{ }^{\circ}\text{C}$ again and adding another large piece of dry ice ($\sim 8\text{ g}$). After mixing at room temperature for an additional 1 hr, the dark orange/red reaction mixture was quenched by (initially dropwise) addition of HCl (2.1 M, 25 mL, 52.5 mmol). Upon quenching, the reaction mixture turned dark brown in color. The product was extracted with 200 mL of CHCl_3 , and the organic layer was washed 3 times with 150 mL of H_2O , then dried with MgSO_4 . The crude product was concentrated, then separated via column chromatography (gradient elution, CHCl_3 then EtOAc, SiO_2 gel 60, $r_f = 0.36$ in EtOAc). ^1H NMR (500 MHz, CDCl_3) δ (ppm): 0.89 (m, 6H), 1.31 (m, 6H), 1.39 (m, 6H), 1.66(m, 4H), 2.78 (t, $J = 5\text{ Hz}$, 2H), 2.80 (t, $J = 5\text{ Hz}$, 2H), 6.94 (d, $J = 5\text{ Hz}$, 1H), 7.03 (d, $J = 5\text{ Hz}$, 1H), 7.15 (m, 3H), 7.19 (d, $J = 5\text{ Hz}$, 1H), 7.70 (s, 1H), 16.10 ppm (s, 1H). FTIR (ATR head) 2950, 2928, 2856, 1660, 1544, 1526, 1502, 1438, 1295, 1279, 1192, 1166, 1092, 1056, 919, 867 cm^{-1} .

Results and Discussion

Synthesis of WO₃

Mesoporous SiO₂ particles were prepared using a soft templating method with the surfactant CTAB under acidic conditions. This method yielded spherical particles with an average particle size of approximately 2 μm, as shown in the SEM micrograph of Figure 3B. This material possessed a large surface area and pore volume, as shown by the results of N₂ physisorption experiments detailed in Table 1.

Mesoporous WO₃ particles were synthesized by hard templating method, with the above described SiO₂ particles as the template. First, a solution containing the WO₃ precursor, ammonium metatungstate (AMT), was added to the dry SiO₂ powder by incipient wetness. The material was then calcined to form the composite material WO₃-SiO₂, of which an SEM micrograph is shown in Figure 3C. The EDS spectrum of this material is shown in Figure 3E. Observed at 1.740 keV is the Si K_α transition, and at 1.775 is the W M_α transition. The signal from Au is due to the Pd/Au coating of the sample stage. The silica was etched away from the composite material with hydrofluoric acid (HF) to yield WO₃ particles. SEM micrographs of this material are shown in Figures 3D and 4. The EDS spectrum of WO₃, acquired at the spot indicated in Figure 3D, is shown in Figure 3F. The absence of the Si K_α peak in the spectrum indicates complete etching of the silica from the material.

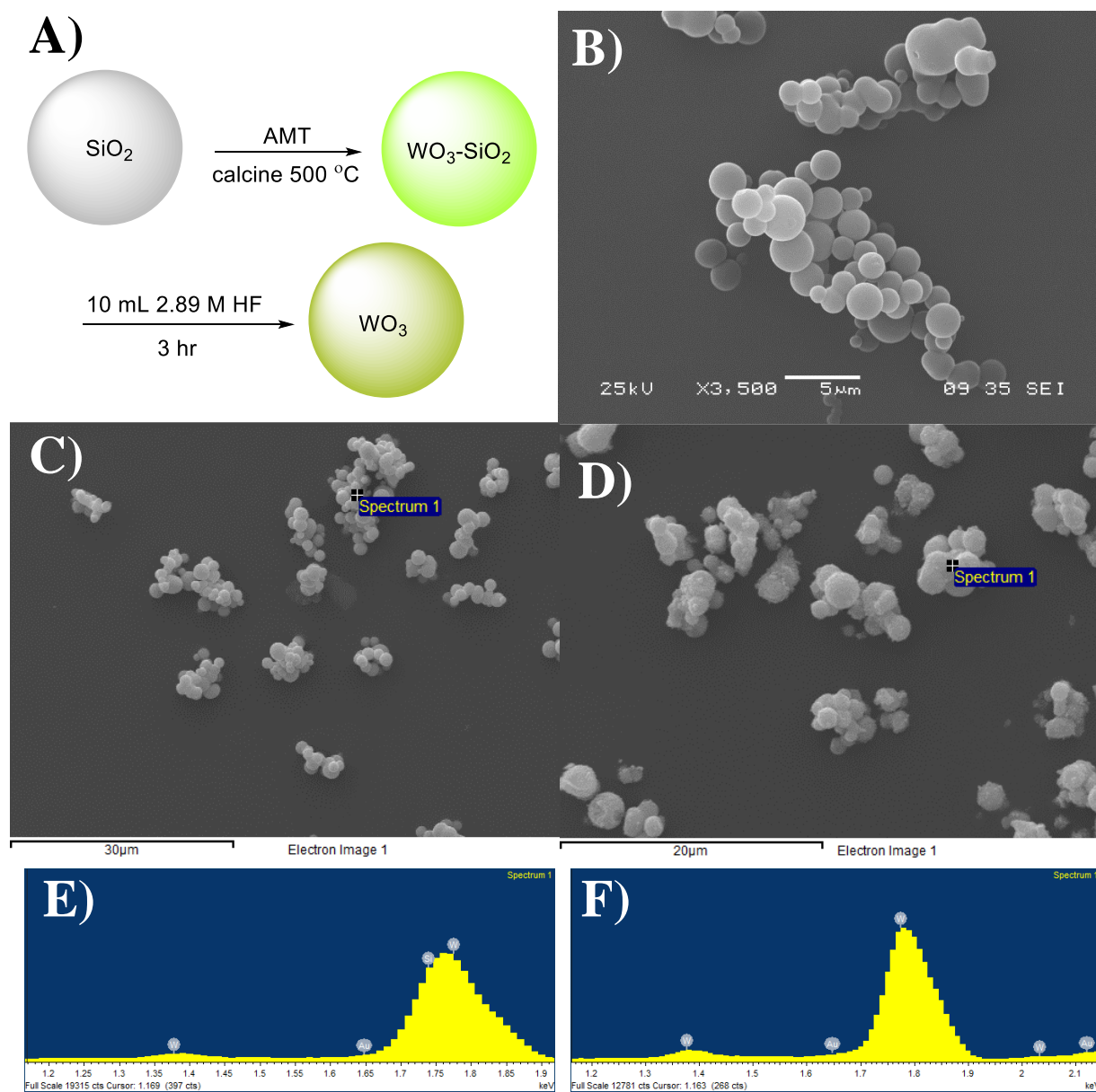


Figure 3: A) Scheme for synthesis of mesoporous WO_3 particles. SEM micrographs of B) SiO_2 , C) $\text{WO}_3\text{-SiO}_2$, and D) WO_3 . EDS Spectra of E) and F) correspond to C) and D), respectively.

Material	SA _{BET} (m ² /g)	d _{pore} (nm)	V _{pore} (mL/g)	Δ% _{m250-600 °C}	Surface Concentration (mmol/g)
SiO ₂	932	7.7	1.65	-	-
WO ₃	60.6	5.5	0.136	-	-
WO ₃ -APTES	53.2	5.0	0.158	5.152 %	0.886 (APTES)
WO ₃ -APTES-FA	36.9	5.8	0.113	6.940 %	0.198 (FA)
WO ₃ -APTES	-	-	-	8.625 %	1.48 (APTES)
WO ₃ -APTES-DH4T	-	-	-	12.290 %	0.375 (DH4T)

Table 1: Results of N₂ physisorption and TGA experiments performed on materials.

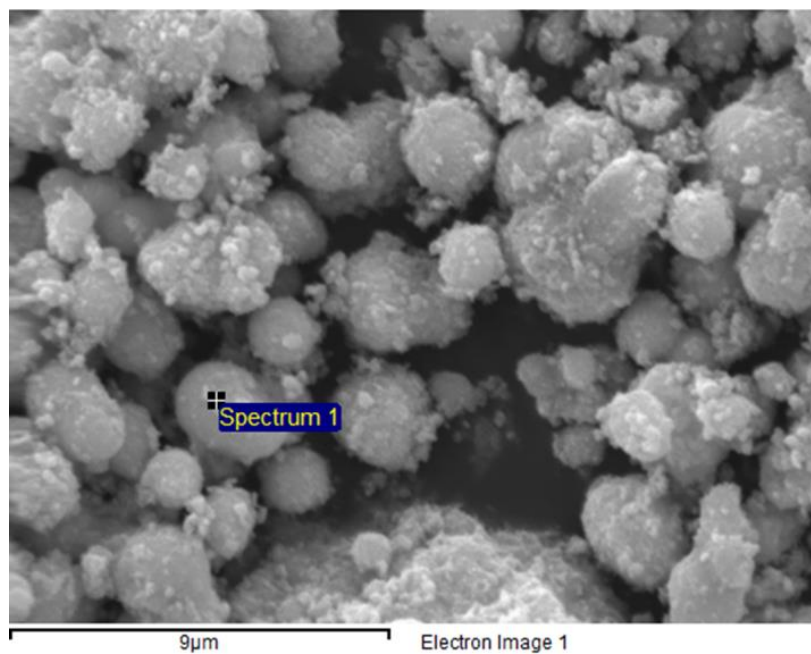


Figure 4: High magnification SEM micrograph of WO₃ (EDS spectrum not shown).

The surface area of WO₃ was much less than that of SiO₂. The SiO₂ template material had a BET surface area of 932 m²/g, whereas WO₃ had a BET surface area of 60.6 m²/g, as

summarized in Table 1. However, this still represents a high surface area material: given that WO_3 has a density of 7.16 g/cm^3 ,⁷ bulk WO_3 particles with a diameter of $2 \mu\text{m}$ would have a surface area of $0.21 \text{ m}^2/\text{g}$. The average pore size of WO_3 particles was determined to be 5.5 nm , although the distribution of pore sizes was very broad. A high magnification SEM micrograph of WO_3 particles is shown in Figure 4. As shown by this image, while most particles are about $2 \mu\text{m}$ in diameter, there exists quite a range of particle sizes, with many particles of submicron diameter. The presence of these small particles, in addition to the porosity of larger particles, contributes to the high surface area measured for the material.

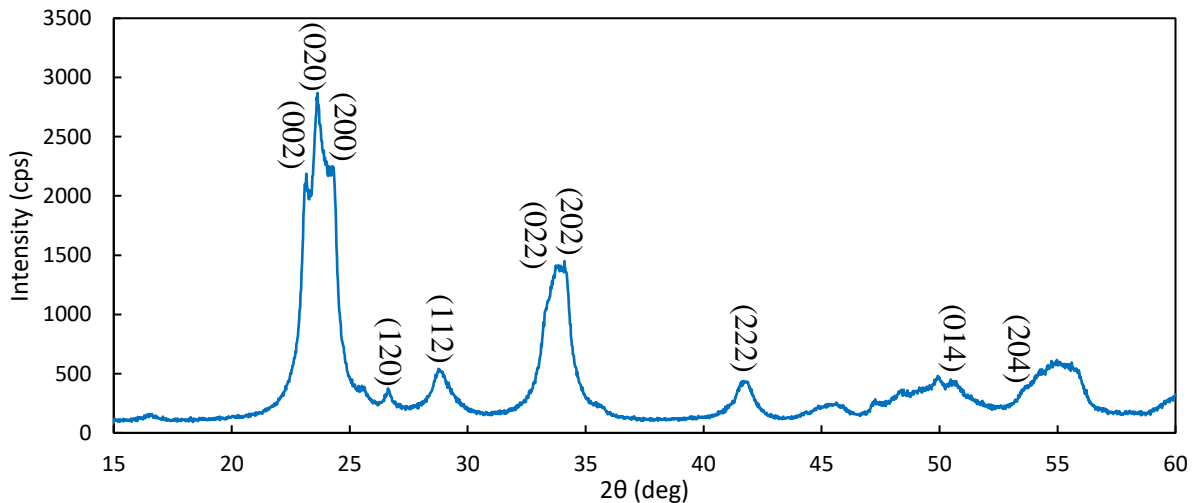


Figure 5: Powder X-ray diffraction pattern for WO_3 .

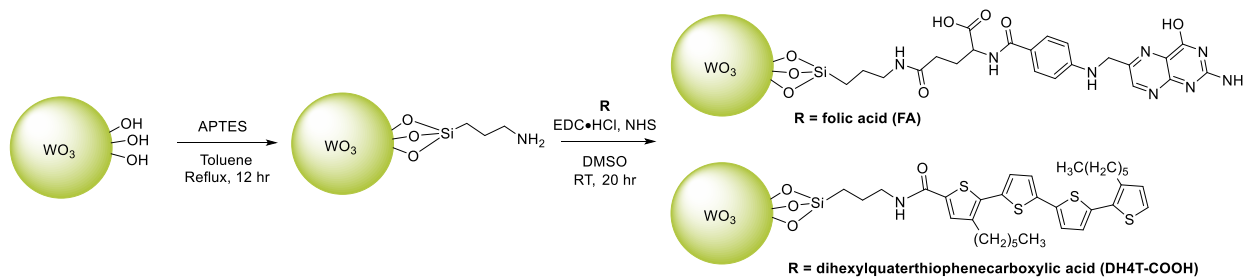
2-theta (deg)	2-theta (rad)	FWHM (deg)	FWHM (rad)	Miller Index	Crystallite Size (nm)
28.79	0.5025	0.853	0.0149	(112)	9.62
41.61	0.7262	0.860	0.0150	(222)	9.89
Average					9.76

Table 2: XRD data used to calculate crystallite size by the Scherrer equation, and obtained crystallite size.

Powder XRD data are shown in Figure 5. The observed diffraction angles are consistent with monoclinic WO_3 of space group Pcnb . The broad peaks are indicative of polycrystallinity. By use of the Scherrer equation, the average crystallite size was calculated. The (112) and (222) peaks were chosen for the calculation, and gave an average crystallite size of 9.76 nm. This crystallite size is much smaller than the particles observed in the SEM micrographs of Figures 3D and 4, which shows that the synthesized WO_3 particles are polycrystalline.

Synthesis of WO_3 -APTES

Mesoporous WO_3 particles were modified with the silane surface anchor aminopropyltriethoxysilane (APTES). Refluxing a suspension of WO_3 particles in toluene with excess APTES gave the functionalized material, denoted WO_3 -APTES. The extent of organic functionalization was determined by thermogravimetric analysis (TGA). Bare WO_3 particles show an approximate 1.5 % decrease in mass from about 225 to 250 °C. This feature could be due to strongly adsorbed water, or condensation of surface hydroxides⁸. To avoid contribution of this feature to the determination of organic content in the powders, the % organic loading was taken to be the change in mass percent from 250 to 600 °C. WO_3 -APTES was shown to possess an organic content of 5.1 % (w/w), which corresponds to a concentration of aminopropyl groups of 0.886 mmol/g (the Si atom was not included in calculation of organic content). The BET surface area of WO_3 -APTES was calculated as 53.2 m²/g. Therefore, the average surface concentration of APTES is 10.0 molecules/nm². The BET surface area of WO_3 -APTES is less than that of WO_3 , which could be due to collapse of pores during reflux, or blocking of N_2 adsorption sites by the APTES molecule. If the latter is true, then the SA_{BET} calculated for bare WO_3 would be more appropriate for use in the calculation of surface concentration of APTES. The surface concentration of APTES is in this manner calculated to be 8.81 molecules/nm².



Scheme 1: Surface modification of WO_3 with APTES and subsequent peptide coupling to obtain chromophore-functionalized WO_3 .

Synthesis of WO_3 -APTES-FA

The APTES surface modification presented an amine functionality that could be used for attachment of chromophore molecules *via* peptide coupling. Folic acid (FA) was peptide coupled to WO_3 -APTES to give WO_3 -APTES-FA. Amide bond formation between FA and WO_3 -APTES was suggested by an increase in organic mass percent. The organic content of WO_3 -APTES-FA was 6.94 % (w/w). Determination of the molar concentration of folic acid in the material is complicated by the presence of 2 different carboxylic acid functional groups on the FA molecule. A fivefold excess of peptide coupling reagents (EDC•HCl and NHS) were used during the reaction, which could allow for activation of both carboxylic acid moieties. The γ carboxylic acid is less sterically hindered, which would allow for more facile reaction than the α carboxylic acid with the surface amine of WO_3 -APTES. This, plus the fact that FA was present at 4/3 the molar amount of surface amine, may make reasonable a proposed structure with FA predominantly bonded to the surface amines solely through the α carboxylic acid. However, the presence of FA bonded through either or both carboxylic acid groups cannot at present be ruled against.

By considering the 0.8864 mmol/g surface concentration of APTES in WO_3 -APTES, it is possible to calculate the theoretical mass percent organic loading that would result from

quantitative consumption of surface amines. The percent by mass of organic loading would be 31.0 % or 19.6 %, for folic acid bonding to the surface amines through one, or both carboxylic acids, respectively. Therefore, based on the mass percent organic loading of 6.940 % in WO_3 -APTES-FA, the percent yield, or percent “completeness” of peptide coupling for WO_3 -APTES-FA is 22.4 %, or 19.6 % for singly bound and doubly bound FA, respectively.

Further insight on organic functionalization is gained by the FTIR spectra of Figure 6. Below approximately 980 cm^{-1} , the spectra are dominated by the bulk W-O modes. Unfunctionalized WO_3 shows resonances at 1396 cm^{-1} and 1614 cm^{-1} , as well as a broad signal at 3381 cm^{-1} . The signal at 1614 cm^{-1} can be attributed to the H-O-H bending of adsorbed water while the signal at 3381 cm^{-1} originates from O-H stretching modes of adsorbed water or surface hydroxides.⁸ Upon surface functionalization with APTES, a new peak at 1503 cm^{-1} is observed, which could be attributed to N-H bending modes⁹⁻¹⁰. A peak at 1300 cm^{-1} also appears, which is possibly due to C-N stretching. The FTIR spectrum of WO_3 -APTES-FA does not show much spectral change, but instead shows larger intensities of the peaks observed in WO_3 -APTES. The lack of new bands could be due to low concentration of FA on the surface.

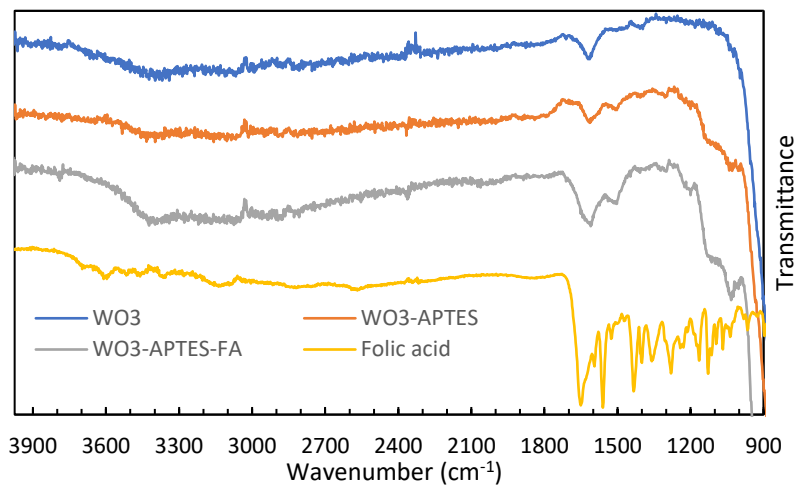
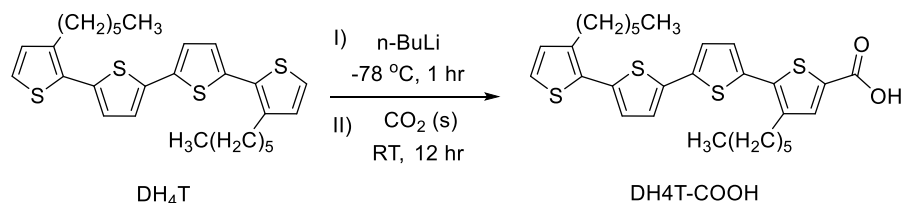


Figure 6: FTIR spectra of WO_3 , WO_3 -APTES, WO_3 -APTES-FA, and FA.

Synthesis of WO₃-APTES-DH4T

Scheme 2: Carboxylation of DH4T.

In order to covalently attach DH4T to APTES through peptide coupling, the DH4T had to first be carboxylated. DH4T was reacted with 1 equivalent of n-butyllithium (nBuLi), which deprotonates the most acidic proton of the molecule: that of the α carbon. Dry ice was then added to the flask, allowing for nucleophilic attack of the carbanion on the CO₂ molecule. Quenching with acid, and separation by separatory funnel and column chromatography gave 3,3''-dihexyl-2,2';5',2'';5'',2'''-quaterthiophene-5-carboxylic acid (DH4T-COOH). The identity of DH4T-COOH was confirmed by ¹H NMR and FTIR. The FTIR spectrum (Figure 8) showed presence of an intense peak at 1660 cm⁻¹, the carboxylic acid C=O stretching frequency, which confirms carboxylation of the molecule. The ¹H NMR spectrum is shown in Figure 7. The observed resonances agree with those reported by Faccetti *et al.*,⁴ from whom this procedure was adapted.

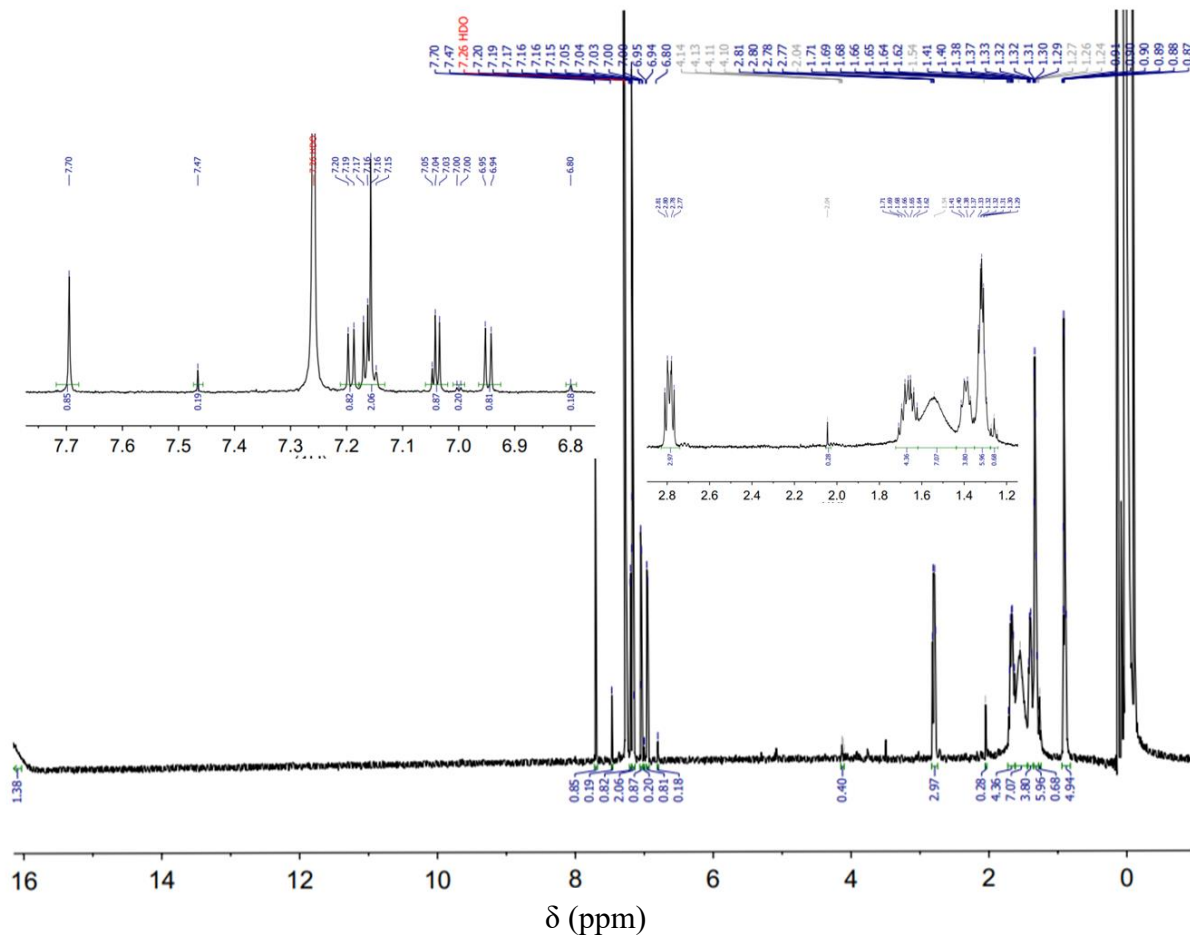


Figure 7: ¹H NMR spectrum of DH4T-COOH.

The WO₃-APTES used to synthesize the DH4T functionalized material had a higher APTES concentration than that used for the FA functionalized material. This is shown by the results of TGA (Table 1): the former had an 8.625 % organic loading by mass, while the latter had only a 5.152 % organic loading. The molar concentration of APTES in the material was 1.48 mmol/g. Peptide coupling of DH4T-COOH to the surface amines yielded material with a very high organic loading of 12.290 % by mass. This implies that 25.3 % of surface amines were consumed, which implies a DH4T concentration of 0.375 mmol/g.

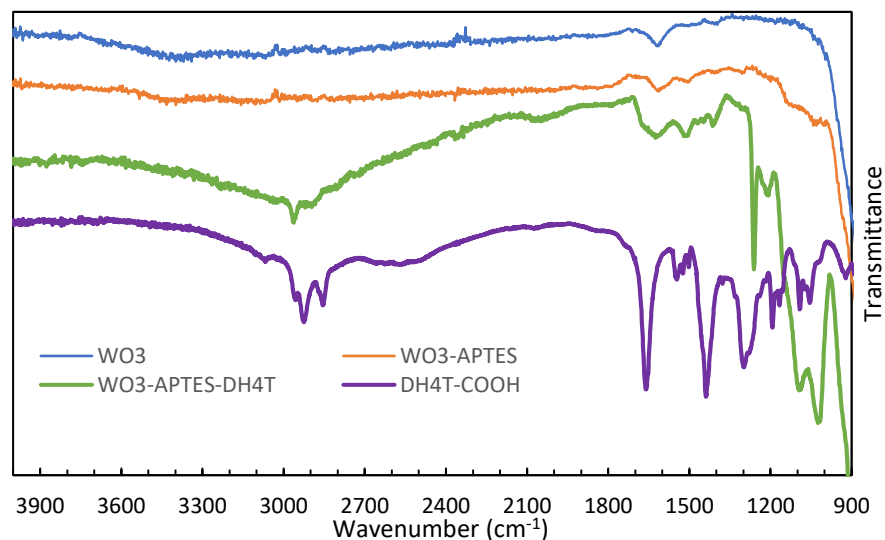


Figure 8: FTIR spectra of WO₃, WO₃-APTES, WO₃-APTES-DH4T, and DH4T-COOH.

The presence of DH4T is clearly seen in the FTIR spectrum of Figure 8. For comparison, the FTIR spectra of WO₃, WO₃-APTES, and DH4T-COOH are shown. However, the FTIR spectrum of WO₃-APTES in Figure 8 is actually that of the material used to synthesize WO₃-APTES-FA, which had a lower concentration of APTES than that used to synthesize WO₃-APTES-DH4T (see Table 1). That is the cause of the apparent jump in intensity of WO₃-APTES-DH4T bands compared to WO₃-APTES bands. An FTIR spectrum of the WO₃-APTES material used for the DH4T-functionalized material likely would have shown identical features to the presented spectrum of WO₃-APTES, but at higher intensities due to the greater surface concentration of APTES. This may have allowed for observation of the N-H and C-H stretches, which are obscured by the O-H stretching modes of surface hydroxides and adsorbed water.

The FTIR spectrum of WO₃-APTES-DH4T confirms the presence of DH4T in the material. Alkyl C-H stretches are observed at 2963 and 2895 cm⁻¹.¹¹⁻¹² An intense resonance is

observed at 1260 cm^{-1} . This could possibly be due to C-N stretch of the amide. Intense bands are also observed at 1090 and 1014 cm^{-1} , the former of which could arise from $C_{\text{ring}}-C_{\text{carbonyl}}$ stretching.¹³ The high intensity of these bands may be in part due to contributions from bulk W-O modes. For the DH4T-COOH molecule, a broad signal at 2550 cm^{-1} , and a sharp, intense signal at 1660 cm^{-1} can be assigned to the O-H and C=O stretches of the carboxylic acid moiety, respectively. The absence of these signals in the WO_3 -APTES-DH4T spectrum indicates successful amide bond formation. The amide C=O stretching mode overlaps with the physisorbed water H-O-H bending mode. Aromatic C=C stretching modes are observed at 1410 , 1445 , and 1470 cm^{-1} .

Optical Properties of WO_3

The bandgap, E_g , of WO_3 may be determined by diffuse reflectance spectroscopy (DRS). The reflectance (R) is converted into $F(R)$, which is proportional to the extinction coefficient, and defined by Equation 2 (in Experimental). WO_3 has an indirect bandgap.¹⁴ The absorption coefficient, and thus $F(R)$ for an indirect bandgap semiconductor are related to the photon energy, E , by the following proportionality :

$$F(R) \propto (E - E_g)^2 \quad 3)$$

Therefore, the bandgap may be estimated by plotting $F(R)^2$ against photon energy, and extrapolating the linear portion of the spectrum to the x axis. This treatment is shown in Figure 9, and gives a bandgap of 2.68 eV (462.6 nm), which lies in between values of 2.6 eV^{14-15} and 2.9 eV^{16} which have previously been reported for WO_3 .

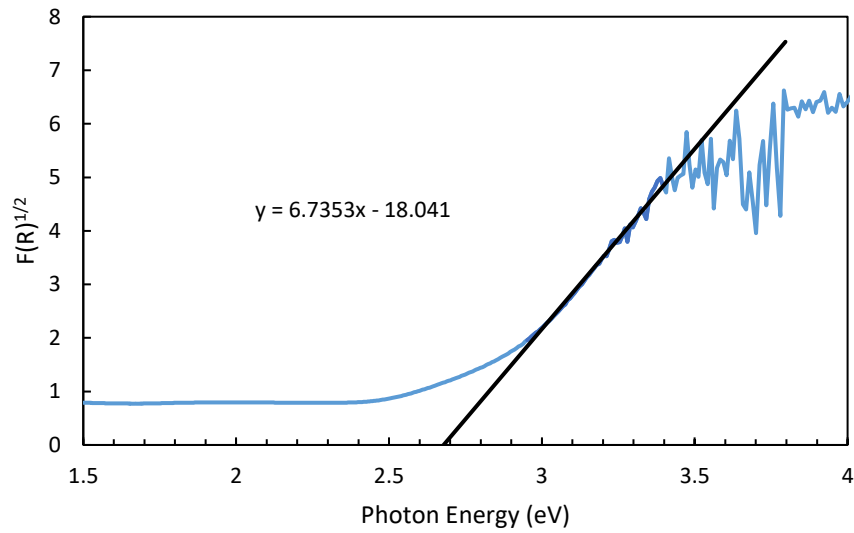


Figure 9: DRS Spectrum of WO₃.

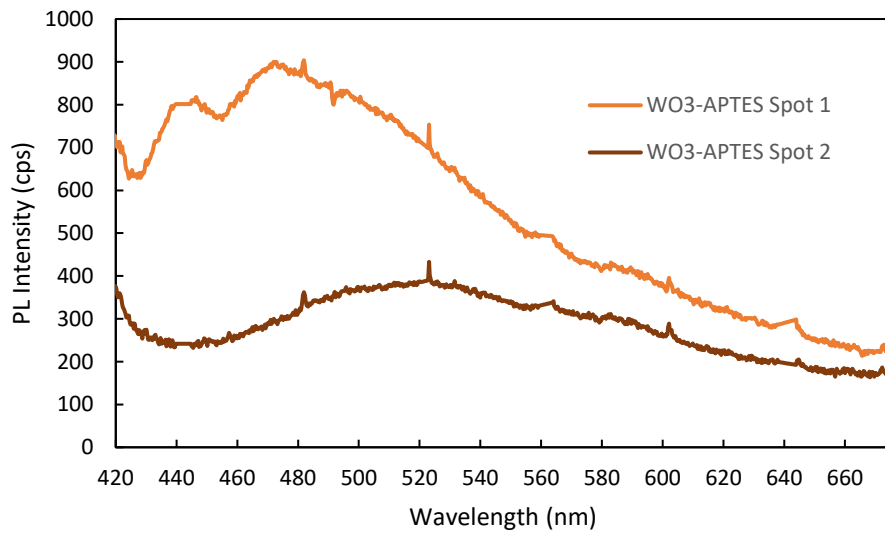


Figure 10: PL spectrum of WO₃-APTES collected at 2 different spots on the sample. Tail of the scattered laser intensity is observed at the high energy edge of the spectrum.

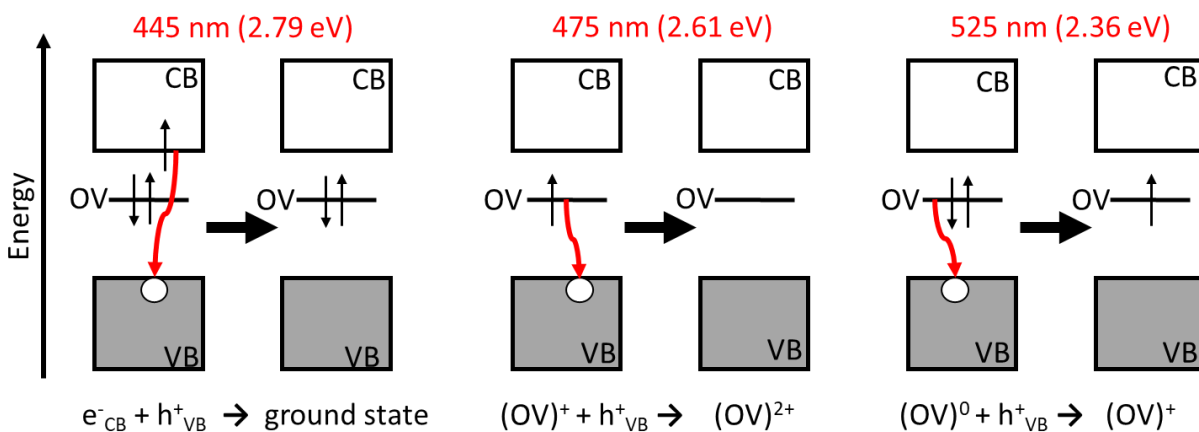
For both WO₃ and WO₃-APTES, the photoluminescence spectrum varied depending on which region of the drop-cast sample was illuminated. Most regions of the glass slide that visually appeared to be coated in sample showed no PL signal. By slowly moving the laser spot

around on the sample, it was possible to find regions of the sample that showed PL when illuminated. The observation of photoluminescence only at certain regions on the sample implies that the drop cast method from ethanol was not sufficient for creating uniform films on the glass. It is observed in the SEM micrograph of Figure 3D that WO_3 particles form aggregates. It may be possible that the PL was only observed when the laser, which was focused to diffraction-limited spot size, was incident with one of these aggregates. Of the sparse regions of the sample that did show PL, the spectrum observed varied between regions. Figure 10 shows the PL spectra from two different spots on a sample of WO_3 -APTES. WO_3 showed identical spectral behavior, indicating that APTES functionalization does not affect the photophysics of WO_3 . Although the scattered intensity of the laser was minimized by cross-polarization, the tail of the laser is still observed at the high energy edge of the spectrum. Spot 1 shows peaks at 445 nm (2.79 eV) and 475 nm (2.61 eV), as well as a shoulder at 525 nm (2.36 eV). Spot 2 only shows a broad PL centered at 525 nm. These spectra show the 3 PL transitions that WO_3 exhibits. The peak at 445 nm is coincident with the bandgap of WO_3 calculated by DRS, and is thus assigned to recombination of thermalized electrons and holes and the conduction and valence band edges, respectively (bandgap recombination). The Peaks at 475 and 525 nm are of less energy than the bandgap, and thus must involve defect states that exist within the bandgap.

WO_3 is known to form substoichiometric phases of formula WO_{3-x} , where x is less than 1, resulting from oxygen vacancies at the surface.¹⁴⁻¹⁵ Tungsten ions that are missing on-top oxygens necessarily exist as W(V) rather than W(VI), as required by charge balance. The presence of W(V) species results in midgap states localized on W. The W(V) ion has a d^1 valence electron configuration, which implies that the oxygen vacancy (OV) states are occupied. These occupied oxygen vacancy (OV) states have been observed in the X-ray photoelectron

spectroscopy of Ar ion-bombarded WO_3 (001) surfaces.¹⁷ The presence of occupied states midgap pins the Fermi level close to the CB minimum.¹⁵ Furthermore, the formation of trough structures on the surface due to OV's is possible,¹⁵ which could allow for the formation of a W(V) OV band.

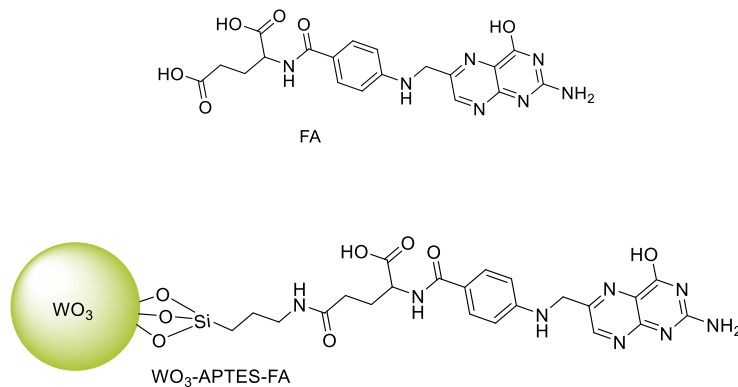
The PL emissions observed at 475 and 525 nm are thus assigned to transitions involving OV states. Johansson *et al.* investigated the PL of nanocrystalline WO_{3-x} thin films,¹⁶ and made assignments based on conclusions of DFT work (with the B3LYP functional) on WO_{3-x} by Wang *et al.*¹⁸ Based on these previous studies, it can be concluded that the peak at 475 nm is due to recombination of an unpaired electron in an OV state with a hole in the VB, and that the peak at 525 nm is due to recombination of a paired electron in an OV state with a hole in the VB. Schematic diagrams of these transitions are shown in Scheme 3. An interesting observation was that the 445 and 475 nm bands always appeared in the spectrum together, and that the 525 nm band sometimes appeared by itself.



Scheme 3: Proposed mechanisms of emission observed in PL spectra of WO_3 and $\text{WO}_3\text{-APTES}$. Only one OV state is shown for simplicity.

The variation in spectrum among different regions of the sample likely arises from particle inhomogeneity, namely varying crystallinity or oxygen vacancy/defect concentration between particles. The WO_3 examined herein was synthesized by calcination of AMT precursor solution within the pores of mesoporous SiO_2 . The calcine program used was a ramp to 500 °C followed by cooling to RT. Had the program included a soak (isothermal) step at 500 °C, perhaps the WO_3 would have crystallized more evenly, resulting in higher homogeneity, and less spectral variation among particles. Other factors that could explain the spectral variation is the differing size of particles, or varying degrees of aggregation of the particles.

Optical Properties of WO_3 -APTES-FA



Scheme 4: Molecular structure of folic acid (FA) and cartoon representation of WO_3 -APTES-FA.

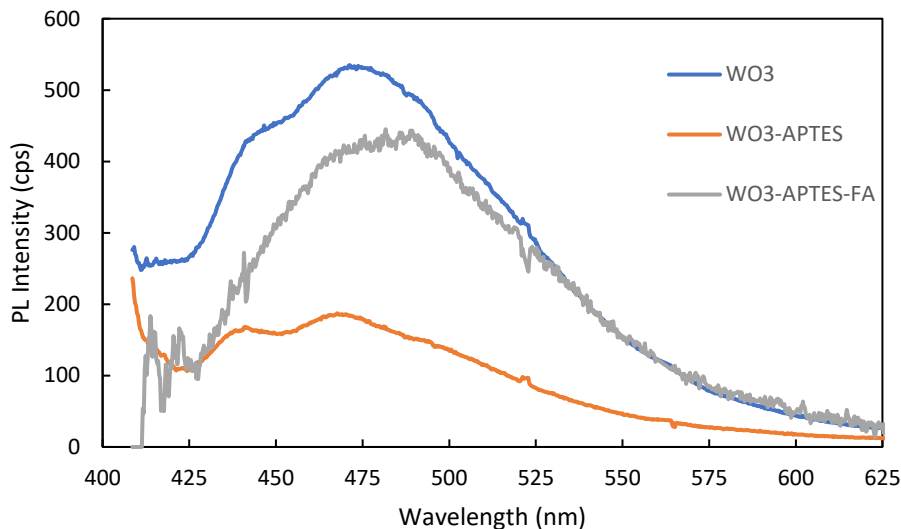


Figure 11: Photoluminescence spectra of WO₃, WO₃-APTES, and WO₃-APTES-FA. Tail of the scattered laser intensity is observed at the high energy edge of the spectrum.

Shown in Figure 11 are the PL spectra of WO₃, WO₃-APTES, and WO₃-APTES-FA. The variation in intensities between WO₃ and WO₃-APTES spectra is due to modest variations in the concentration of suspension used for drop casting. Functionalization of the material with FA leads to no significant change in spectrum; no increase in emission intensity is seen, and the emission wavelength is not significantly shifted from the WO₃. It is therefore concluded that the PL observed for WO₃-APTES-FA is simply emission from the particle, and that the presence of folic acid does not affect the PL of the particle, when excited at 405 nm.

The lack in changes to the PL spectrum of WO₃ upon FA functionalization could be due to the small concentration of the molecule on the surface. Furthermore, FA does not absorb light at 405 nm, as shown in the absorbance spectrum of Figure 12. Perhaps if the laser light was on resonance with an electronic transition of the molecule, WO₃-APTES-FA would've shown a more interesting PL spectrum.

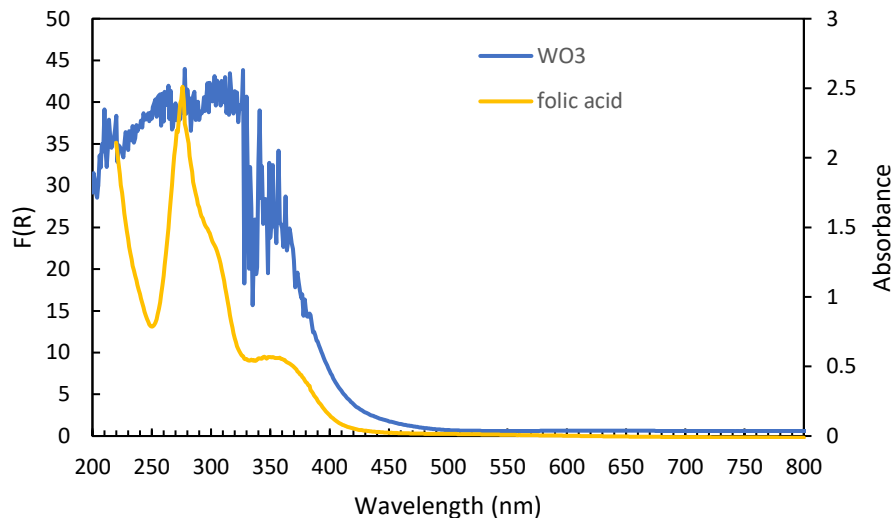
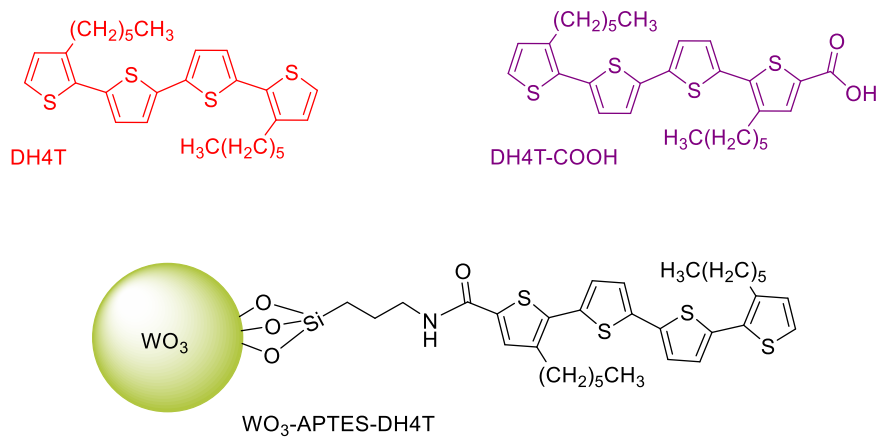


Figure 12: DRS and absorption spectrum of WO₃ and FA, respectively.

Optical Properties of WO₃-APTES-DH4T



Scheme 5: Molecular structures of dihexylquaterthiophene (DH4T) and dihexylquaterthiophenecarboxylic acid (DH4T-COOH) and cartoon representation of WO₃-APTES-DH4T.

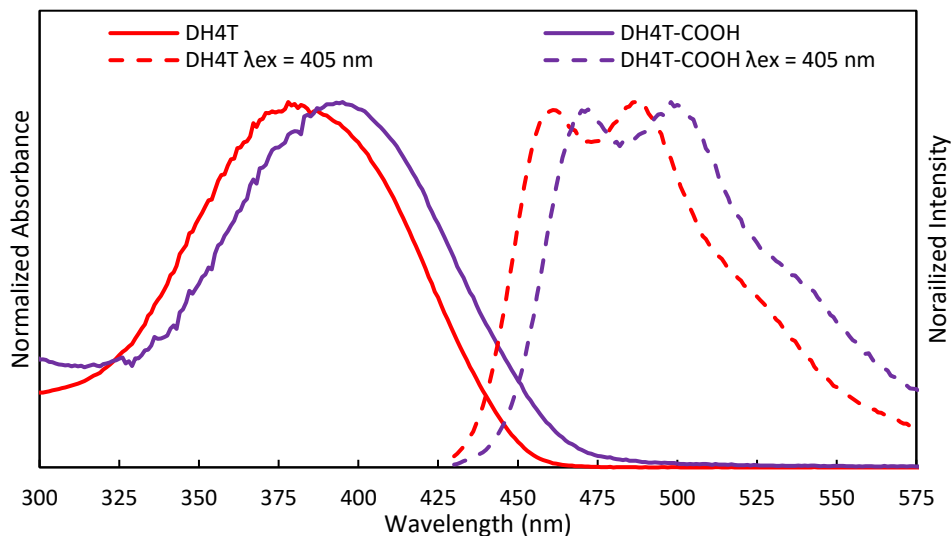


Figure 13: Normalized absorption and emission spectra of DH4T and DH4T-COOH in DMSO.

The absorption and fluorescence spectra of DH4T and DH4T-COOH are shown in Figure 13. The peak wavelengths of absorption and emission are red-shifted for DH4T-COOH compared to the parent compound. This is expected due to the electron withdrawing substituent, and larger π system of DH4T-COOH. It is assumed that the amide substituent in WO_3 -APTES-DH4T has a similar effect on the absorption/emission spectra of DH4T.

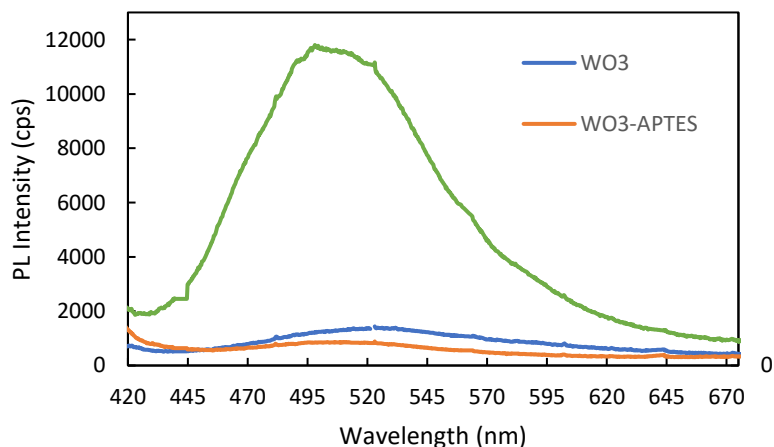


Figure 14: PL spectra of WO_3 , WO_3 -APTES, and WO_3 -APTES-DH4T. Tail of the scattered laser intensity is observed at the high energy edge of the spectrum.

The PL spectra of WO_3 , WO_3 -APTES and WO_3 -APTES-DH4T are shown in Figure 14. The latter shows an intense PL centered at 505 nm, with a shoulder at 470 nm. Although the amount of material on the glass slide varied between experiments, the tenfold increase in PL intensity cannot be explained by the small changes in concentration. Clearly, the presence of the DH4T molecule increases the PL of the WO_3 system. The PL from WO_3 -APTES-DH4T appears to show contribution from the molecule-centered emission. However, the PL also shows some component that is red shifted with respect to the molecular transition. It is possible that this is contribution from transitions within WO_3 involving OV states.

Curve fitting was performed on the PL spectrum WO_3 -APTES-DH4T in order to decompose the spectrum into contributions from WO_3 -APTES and DH4T. The tail of the laser was modeled by a Lorentzian function, whereas the electronic transitions of WO_3 -APTES and DH4T-COOH were modeled with Gaussian functions. Spectra were smoothed *via* Loess regression prior to fitting.

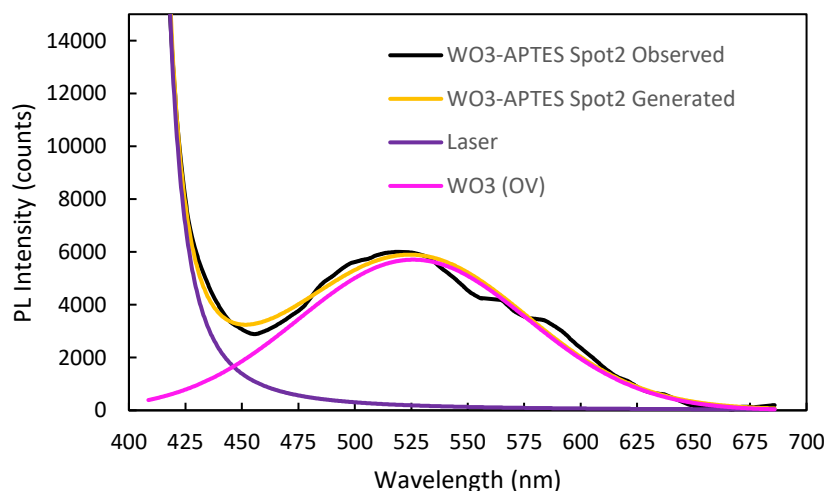


Figure 15: Decomposition of PL spectrum of WO_3 -APTES Spot 2.

Peak	Type	Intensity (counts)	λ_0 (nm)	FWHM (nm)
Laser	Lorentzian	60781.39	406.5928	6.641364
WO ₃ (OV)	Gaussian	5705.836	525.8415	50.64225

Table 3: Fitting parameters for PL spectrum of WO₃-APTES Spot 2.

Figure 15 shows the decomposition of the spectrum of WO₃-APTES Spot 2. This spectrum only shows contribution from the (OV)⁰ to VB transition. A peak wavelength of 525.84 nm was found for this transition. The spectrum is not well reproduced in the region of approximately 540 to 610 nm. This is likely due to artifacts in the raw spectrum. The data points of these “spike” artifacts were deleted prior to smoothing, but caused the appearance of apparent features in the spectrum.

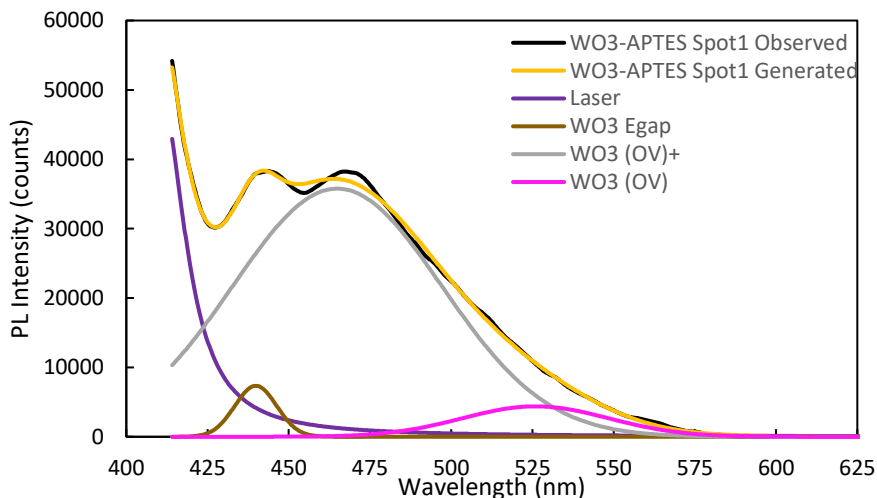


Figure 16: Decomposition of PL spectrum of WO₃-APTES Spot 1.

Peak	Type	Intensity (counts)	λ_0 (nm)	FWHM (nm)
Laser	Lorentzian	48337.2229	410.955413	8.87829637
WO ₃ Egap	Gaussian	7340.04837	439.85139	6.4507034
WO ₃ (OV)+	Gaussian	35766.6605	464.927722	32.2210073
WO ₃ (OV)	Gaussian	4383.65905	525.91623	22.5581764

Table 4: Fitting parameters for PL spectrum of WO₃-APTES Spot 1.

The PL spectrum of WO_3 -APTES at Spot 1 (Figure 16) showed contribution from CB to VB, $(\text{OV})^+$ to VB, and $(\text{OV})^0$ to VB transitions. The peak wavelength of 525.84 nm for the $(\text{OV})^0$ to VB transition, determined from the fitting of the PL spectrum at Spot 2, was used in the fitting of Spot 1, and heavily constrained such that it would not deviate more than 0.05 % of its original value. The amplitude and FWHM of this transition, however, were allowed to vary. It was found that the contribution from bandgap recombination, centered at 439.85 nm, was rather small. The majority of the emission was found to arise from the $(\text{OV})^+$ to VB transition, which was centered at 464.92 nm. The $(\text{OV})^0$ to VB transition in this fitting converged to 525.92 nm. The three WO_3 transitions and the laser peak did a poor job reproducing the doublet appearance of the observed PL spectrum. Specifically, the peak wavelength of the $(\text{OV})^+$ to VB transition in the generated spectrum is slightly blue shifted compared to the observed spectrum. The region around the maximum of the $(\text{OV})^+$ to VB peak would perhaps be better produced with a narrower FWHM of said peak, and invocation of another transition to the red of it. However, this fitting was considered satisfactory, and the peak wavelengths found were used, and fixed, in the subsequent fitting of WO_3 -APTES-DH4T.

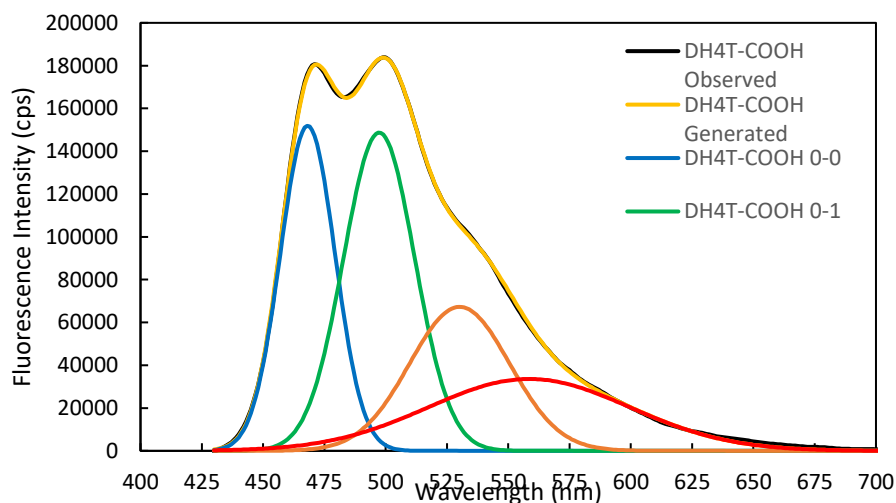


Figure 17: Decomposition of fluorescence spectrum of DH4T-COOH.

Peak	Type	Intensity (counts)	λ_0 (nm)	FWHM (nm)
DH4T-COOH 0-0	Gaussian	1.519E+05	468.19932	11.15875
DH4T-COOH 0-1	Gaussian	1.4875E+05	497.345985	14.5202197
DH4T-COOH 0-2	Gaussian	67267.398	530.169395	20.3799887
DH4T-COOH 0-3	Gaussian	33591.1269	558.534448	41.1062571

Table 5: Fitting parameters for fluorescence spectrum of DH4T-COOH.

The fluorescence spectrum of DH4T-COOH was decomposed into the first 4 vibronic transitions of DH4T-COOH (Figure 17). The peak wavelengths of the 0-0, 0-1, 0-2, and 0-3 transitions were found to be 468.20, 497.35, 530.17, and 558.53 nm, respectively. It was found that the FWHM of the vibronic transitions increased with wavelengths. The obtained peak wavelengths were used and fixed in the fitting of WO₃-APTES-DH4T.

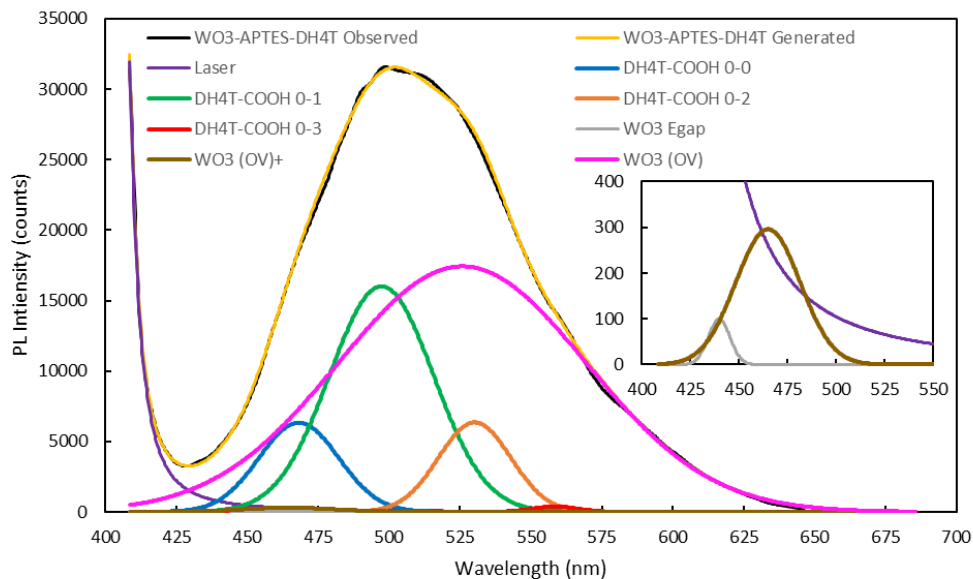


Figure 18: Decomposition of PL spectrum of WO₃-APTES-DH4T. For clarity, all traces but ‘Laser,’ ‘WO₃ Egap,’ and ‘WO₃ (OV)+’ are omitted from inset.

Peak	Type	Intensity (counts)	λ_0 (nm)	FWHM (nm)
Laser	Lorentzian	63941.31	404.7282	3.857802
WO3 Egap	Gaussian	99.60627	439.8514	5.56803
WO3 (OV) ⁺	Gaussian	296.0874	464.9277	16.58939
DH4T-COOH 0-0	Gaussian	6324.931	468.1993	14.07568
DH4T-COOH 0-1	Gaussian	16011.44	497.3452	18.33368
WO3 (OV)	Gaussian	17427.6	525.8414	43.73451
DH4T-COOH 0-2	Gaussian	6354.226	530.1694	12.74667
DH4T-COOH 0-3	Gaussian	381.8254	558.5345	7.91021

Table 6: Fitting parameters for PL spectrum of WO₃-APTES-DH4T.

The PL spectrum of WO₃-APTES-DH4T was decomposed into contributions from WO₃-APTES and DH4T-COOH. The peak wavelengths, as determined from the previously described fits of these components, were fixed, although the amplitudes and FWHMs were allowed to vary. As shown by Figure 18, The greatest contribution to the emission comes from the molecular fluorescence and the WO₃ transition originating from the (OV)⁰ state. The contribution from bandgap recombination and the transition originating from the (OV)⁺ state were found to be extremely small, as shown by the inset of Figure 18 (all traces but ‘Laser,’ ‘WO3 Egap,’ and ‘WO3 (OV)⁺’ are omitted from inset, for clarity). The OV⁺ to VB transition is nearly resonant with the DH4T-COOH 0-0 transition. Therefore, the observed spectrum could have also been well reproduced by greater contribution from the (OV)⁺ transition, and less contribution from the 0-0 transition. However, this model would give an unrealistically small ratio of the intensities of the first two vibronic peaks, I_{0-0} / I_{0-1} . Indeed, this ratio was close to 1 in the fluorescence spectrum of the molecule. The peak shapes and relative intensities of the bandgap recombination and (OV)⁺ to VB transition are similar to that observed for WO₃-APTES Spot 1, which further supports the validity of this fit, and may suggest that the presence of surface-bound DH4T does not affect these transitions. It is clear, however, that the (OV)⁰ to VB transition is significantly enhanced by the presence of DH4T, based on its large contribution to the spectrum

in Figure 18, and the relative PL intensities of the functionalized and unfunctionalized material in Figure 14.

A comparison of the DRS and absorption spectra of WO_3 and DH4T-COOH is shown in Figure 19A. Figure 19B shows the redox potentials of WO_3 ³ and DH4T.¹⁹ The HOMO and LUMO (or CB edge and VB edge) can be approximated by the oxidation and reduction potentials, respectively. Based on the redox potentials and absorption spectra of Figure 19, a PL mechanism may be proposed.

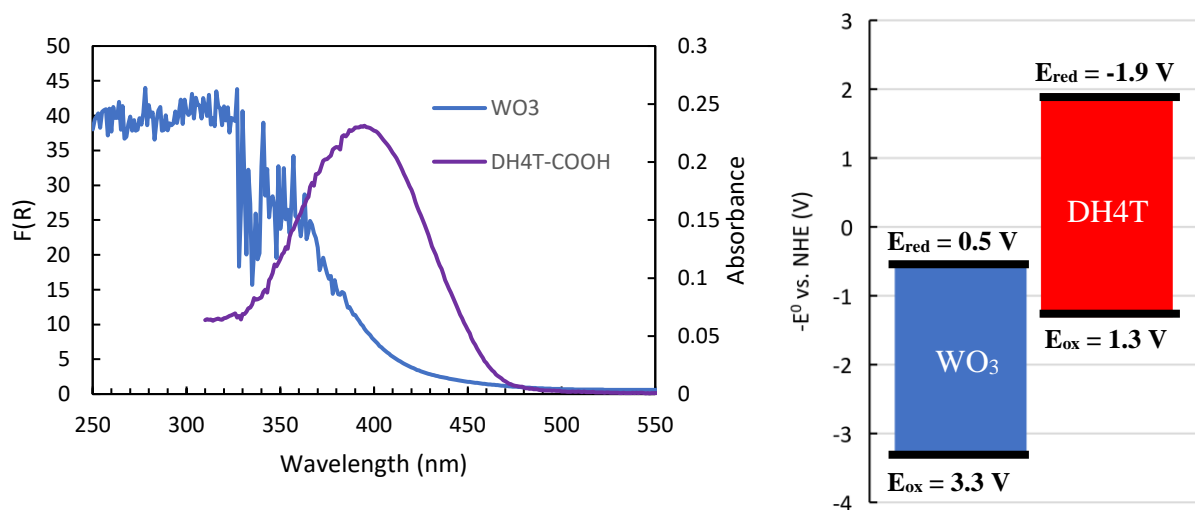
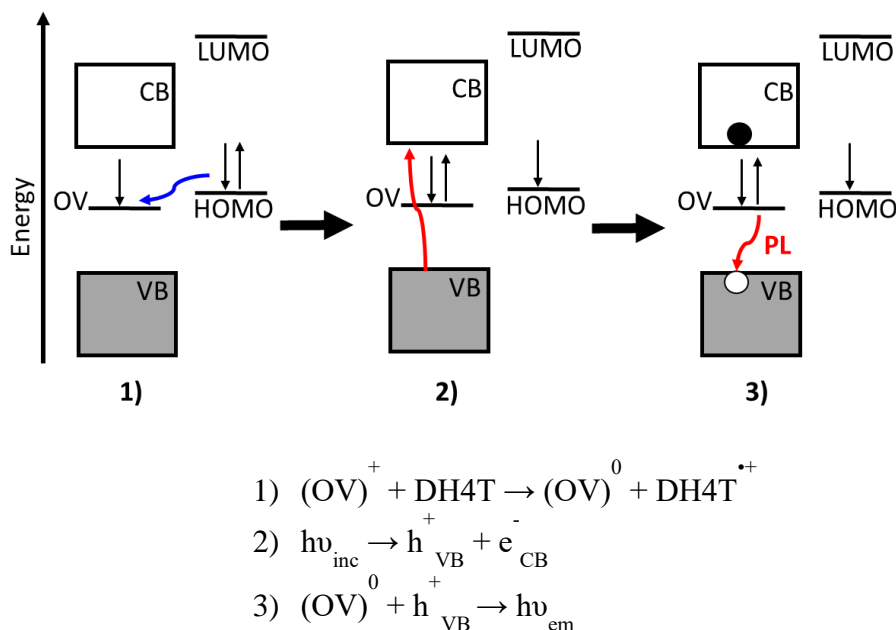


Figure 19: A) DRS and absorption spectrum of WO_3 and DH4T-COOH, respectively. B) Redox potentials of WO_3 ³ and DH4T¹⁹ against normalized hydrogen electrode (NHE).

In addition to showing emission from the molecule, WO_3 -APTES-DH4T shows enhanced PL intensity of the $(\text{OV})^0$ to VB transition of WO_3 , centered at 525.8 nm. This transition involves the reaction $(\text{OV})^0 + h^+_{\text{VB}} \rightarrow (\text{OV})^+$. Therefore, a PL mechanism must involve increased generation of these initial species due to surface-bound DH4T. As shown by the redox potentials of Figure 19, the valence band of WO_3 is sufficiently low in energy such that hole transfer from the molecule to the solid is unfeasible. Therefore, the h^+_{VB} species must be generated by photoexcitation. Quaterthiophene is often used as a p-type material in electronics, due to its large

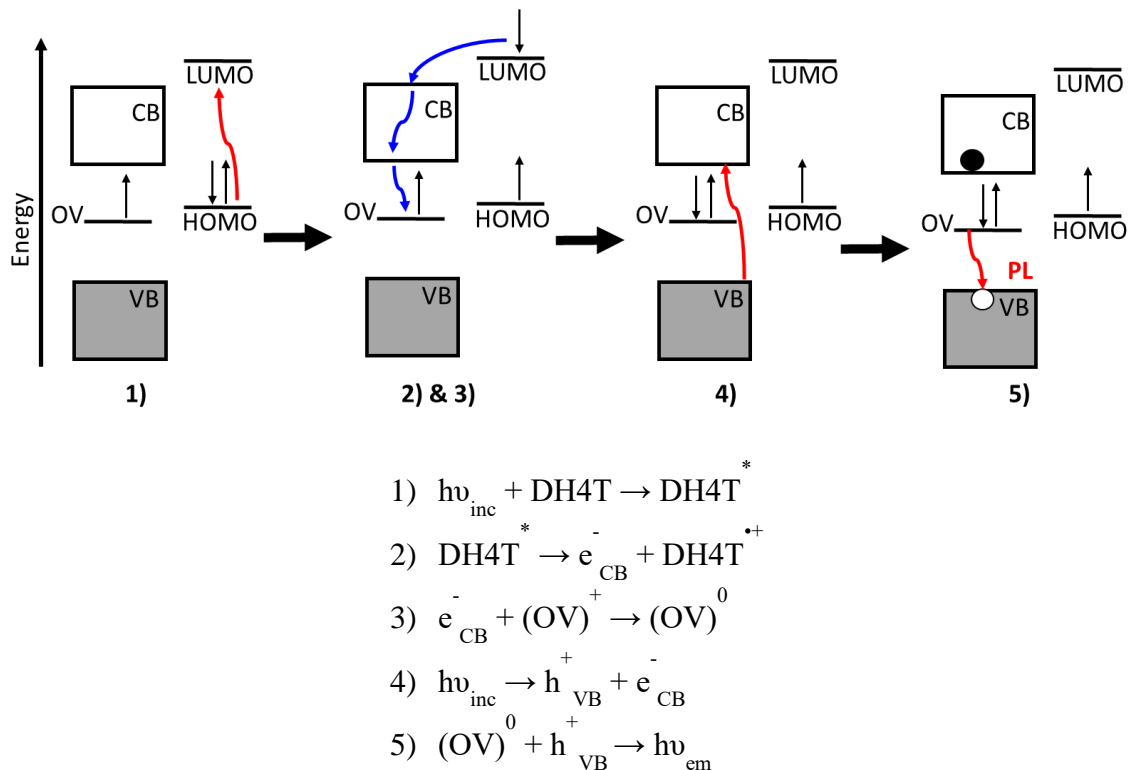
positive oxidation potential. Furthermore, the electron withdrawing substituent of DH4T-COOH (or the amide substituent of the surface bound DH4T) likely lowers the energy of the HOMO, making it a more potent hole acceptor. The HOMO of DH4T lies 0.8 V below the CB of WO₃, based on the redox potentials of Figure 19. The energy of this orbital likely lies within that of the OV band of WO₃. Therefore, hole transfer from the OV states of WO₃ to the HOMO of surface-bound DH4T is conceivable. This ground state hole transfer is the essential sensitization step of Mechanism 1, which is detailed in Scheme 5.



Scheme 5: Proposed Mechanism 1 of WO₃-APTES-DH4T PL emission. Only one OV state is shown for simplicity.

As shown by the absorption spectrum of Figure 19A, the HOMO-LUMO transition of DH4T-COOH is resonant with the 405 nm laser line. Therefore, a high concentration of electronically excited, surface-bound DH4T likely exists in the laser-irradiated region of the WO₃-APTES-DH4T sample. Therefore, this species is a likely player in the photoluminescence mechanism. Mechanism 2, which features this species, involves electron transfer from excited DH4T to the CB, subsequent thermal relaxation of the electron to the band edge, and transfer to

the $(OV)^+$ state. Electrons in the filled OV state then combine with photogenerated holes to give the observed photoluminescence. Mechanism 2 is shown in Scheme 6. Step 3, which involves electron transfer from the CB to an OV state, is drawn as a nonradiative transition, although it could possibly be radiative; the energy of the transition likely lies lower than the spectral range of the PL experiments.



Scheme 6: Proposed Mechanism 2 of WO_3 -APTES-DH4T PL emission. Only one OV state is shown for simplicity.

Although further studies are needed to support or discredit either mechanism, Mechanism 2 is proposed to be the dominant one. Based on the absorption spectrum of DH4T-COOH shown in Figure N, excitation of surface-bound DH4T is likely a frequent process upon irradiation with the 405 nm laser. Furthermore, excited state DH4T is likely a more potent reductant than ground state DH4T, as the electron is more destabilized in the LUMO. It is therefore speculated that DH4T acts to sensitize WO_3 in this system by transfer of an excited electron to the CB, which

then thermalizes to the band edge, relaxes to a partially occupied OV state, then combines with a photogenerated hole in the CB.

Possible Consequences on Photocatalytic Activity

The (thermal) catalytic activity of WO_3 arises from acidic sites that, for example, are capable of dehydration of methanol to form dimethyl ether.²⁰ Additional activity towards oxidation of organic molecules arises from the lability of surface oxygens, and the ability to form the partially reduced substoichiometric species WO_{3-x} .^{14, 20} Labile surface oxygens can insert into hydrocarbons, thus oxidizing them. Regeneration of the catalyst is accomplished by reaction of the oxygen vacancy with an oxidant in the reaction mixture. The selectivity towards oxidation products is greatly increased under photocatalytic conditions. Bandgap irradiation leads to formation of electron-hole pairs. Upon dissociation, these charge carriers may become trapped in surface states. In other words, the photogenerated electrons or holes are able to reduce or oxidize, respectively, surface-adsorbed species. Oxidation of surface hydroxides by holes can lead to reactive hydroxide radicals, which can then react with substrate. Alternatively, surface-adsorbed substrates can also directly accept the photogenerated electron or hole.

Former work in the Landry group by DePuccio²¹ investigated the photocatalytic activity of WO_3 towards methanol (MeOH) under aerobic conditions. A feed of MeOH-saturated N_2 gas mixed with air was passed over the catalyst, which was deposited on a glass slide and irradiated with a Xe-arc lamp. The dehydration product, dimethyl ether, as well as the oxidation products of formaldehyde (FM), methyl formate (MF), and carbon dioxide were observed. Formation of H_2O also resulted from reduction of O_2 in the stream. The ratio e^-/h^+ was defined as the ratio of

reduction products (H_2O) to oxidation products ($\text{FM} + \text{MF} + \text{CO}_2$). The e^-/h^+ ratio was found to be 0.44 for WO_3 .

The enhanced PL from WO_3 -APTES-DH4T may indicate that this material could possess modified photocatalytic activity. Mechanisms 1 and 2 proposed in the preceding section involve transfer of holes from WO_3 to DH4T. This could change the relative selectivity of the material towards reduction and oxidation products. Specifically, hole transfer to DH4T could cause an increase in the e^-/h^+ ratio. Both mechanisms ultimately involve electron transfer to the OV states of WO_3 , which could allow for more facile reaction of oxygen vacancies with molecular oxygen in the gas feed.

A limiting effect of DH4T functionalization on the photocatalytic activity of WO_3 would be the loss of active sites due to APTES bonding to the surface. However, perhaps some optimization of surface modification could be achieved that maximizes the sensitization by DH4T while minimizing the number of surface sites bonded to APTES.

Conclusion

Mesoporous WO_3 microparticles, synthesized *via* a hard templating method utilizing mesoporous SiO_2 as the template, were successfully functionalized with the π -conjugated organic molecules FA and DH4T. The silane anchor, APTES, allowed for covalent attachment to the surface, and provided an amine functional group for attachment to the FA and DH4T-COOH by peptide coupling.

WO_3 -APTES-DH4T showed intense PL when excited with a 405 nm laser. Curve fitting suggested that the PL contained contribution from the molecular fluorescence, as well as the transition from doubly occupied OV states to the VB, centered at 525.8 nm. Because this

transition involved combination of the neutral $(OV)^0$ state electrons and h^+_{VB} , it was proposed that the presence of surface-bound DH4T increases the intensity of this transition by generation of the $(OV)^0$ state. The proposed mechanism by which this occurred involved transfer of an excited electron from the LUMO of DH4T to the CB of WO_3 , and subsequent relaxation of the electron to fill a partially filled $(OV)^+$ state. The electron in the filled $(OV)^0$ state could then combine with photogenerated h^+_{VB} , causing the observed PL signal. This filling of OV states and hole transfer to DH4T could cause a change in photocatalytic activity of the material, by increasing the reactivity of oxygen vacancies towards oxidants in the reaction mixture, thus causing an increase in the production of reduction products.

The presence of surface-bound folic acid in WO_3 -APTES-FA did not change the PL properties of WO_3 . This may be due to the lower surface concentration of FA on WO_3 -APTES-FA than DH4T on WO_3 -APTES-DH4T. Another factor that likely contributes more is the fact that no electronic transitions of FA are resonant with the 405 nm laser. It is possible that novel PL behavior could be exhibited from the WO_3 -APTES-FA, if excited at shorter wavelengths.

Acknowledgements

I would like to thank my advisor, Dr. Christopher Landry, for his support and guidance throughout my two and a half years in his group. He has been a fantastic mentor, and I will miss our intellectually-stimulating conversations. I would like to thank the members of the Landry group, past and present, who have taught and guided me in the laboratory, notably Aaron Vrolijk, Robert Tracy, Jenna Taft, and Michelle Dipinto. I would like to extend a special thanks to Libin Liang for performing the photoluminescence spectroscopy experiments with me.

Brandon Ackley and Ben Kagan are acknowledged for assistance in the carboxylation of dihexylquaterthiophene. I would also like to thank my committee members, Dr. Madalina Furis and Dr. Matthew Liptak for their commitment and patience. Further gratitude is extended to Dr. Furis for the fruitful collaboration, informative discussions on semiconductor physics, and assistance in curve fitting. This work was funded by the University of Vermont College of Arts and Sciences and Department of Chemistry through the APLE award.

References

1. Galoppini, E., *Coordin Chem Rev* **2004**, *248* (13-14), 1283-1297.
2. Materna, K. L.; Crabtree, R. H.; Brudvig, G. W., *Chem Soc Rev* **2017**.
3. Radha, R.; Srinivasan, A.; Manimuthu, P.; Balakumar, S., *Journal of Materials Chemistry C* **2015**, *3* (39), 10285-10292.
4. Tanaka, K.; Takimiya, K.; Otsubo, T.; Kawabuchi, K.; Kajihara, S.; Harima, Y., *Chem Lett* **2006**, *35* (6), 592-593.
5. Turkowski, V.; Babu, S.; Le, D.; Kumar, A.; Haldar, M. K.; Wagh, A. V.; Hu, Z.; Karakoti, A. S.; Gesquiere, A. J.; Law, B.; Mallik, S.; Rahman, T. S.; Leuenberger, M. N.; Seal, S., *ACS Nano* **2012**, *6* (6), 4854-63.
6. López, R.; Gómez, R., *Journal of Sol-Gel Science and Technology* **2011**, *61* (1), 1-7.
7. Latham, R. V.; Cook, S., *Surface Science* **1987**, *179* (2), 503-526.
8. Kanan, S. M.; Lu, Z.; Cox, J. K.; Bernhardt, G.; Tripp, C. P., *Langmuir* **2002**, *18* (5), 1707-1712.
9. Ukaji, E.; Furusawa, T.; Sato, M.; Suzuki, N., *Applied Surface Science* **2007**, *254* (2), 563-569.
10. Ta, T. K. H.; Tran, T. N. H.; Tran, Q. M. N.; Pham, D. P.; Pham, K. N.; Cao, T. T.; Kim, Y. S.; Tran, D. L.; Ju, H.; Phan, B. T., *Journal of Electronic Materials* **2017**, *46* (6), 3345-3352.
11. Martines, F.; Neculqueo, G.; Veas, M. E., *Boletín de la Sociedad Chilena de Química* **2000**, *45*, 53-57.
12. Drapcho, D.; Hasegawa, T., *Spectroscopy: Solutions for Materials Analysis* **30** (8), 31-38.
13. Karthick, T.; Balachandran, V.; Perumal, S., *Spectrochimica Acta Part A: Molecular and Biomolecular Spectroscopy* **2015**, *141*, 104-112.
14. Bullett, D. W., *Journal of Physics C: Solid State Physics* **1983**, *16* (11), 2197.
15. Jones, F. H.; Rawlings, K.; Foord, J. S.; Egdell, R. G.; Pethica, J. B.; Wanklyn, B. M. R.; Parker, S. C.; Oliver, P. M., *Surface Science* **1996**, *359* (1), 107-121.
16. Johansson, M. B.; Zietz, B.; Niklasson, G. A.; Österlund, L., *Journal of Applied Physics* **2014**, *115* (21), 213510.
17. Dixon, R. A.; Williams, J. J.; Morris, D.; Rebane, J.; Jones, F. H.; Egdell, R. G.; Downes, S. W., *Surface Science* **1998**, *399* (2), 199-211.
18. Wang, F.; Di Valentin, C.; Pacchioni, G., *Physical Review B* **2011**, *84* (7), 073103.

19. Facchetti, A.; Yoon, M.-H.; Stern, C. L.; Hutchison, G. R.; Ratner, M. A.; Marks, T. J., *Journal of the American Chemical Society* **2004**, *126* (41), 13480-13501.
20. DePuccio, D. P.; Ruíz-Rodríguez, L.; Rodríguez-Castellón, E.; Botella, P.; López Nieto, J. M.; Landry, C. C., *The Journal of Physical Chemistry C* **2016**, *120* (49), 27954-27963.
21. DePuccio, D. P.; Landry, C. C., *Catal Sci Technol* **2016**, *6* (20), 7512-7520.